Chemical Engineering Journal 149 (2009) 242–248

Contents lists available at ScienceDirect

Chemical Engineering Journal

journal homepage: www.elsevier.com/locate/cej

Characterization of the cation-exchanged bentonites by XRPD, ATR, DTA/TG analyses and BET measurement

B. Caglar, B. Afsin*, A. Tabak, E. Eren

Department of Chemistry, Faculty of Arts and Sciences, Ondokuz Mayis University, Kurupelit, Samsun 55139 Turkey

ARTICLE INFO

Article history:
Received 23 July 2008
Received in revised form 15 October 2008
Accepted 30 October 2008

Keywords:
Bentonite
Cation exchange
XRPD
ATR
Thermal analysis
Surface area

ABSTRACT

X-ray powder diffraction (XRPD) analysis demonstrated that the main montmorillonite component of Unye bentonite was more effective in the Pb^{2+}, Cu^{2+}, Ni^{2+}, Co^{2+}, Zn^{2+}, Al^{3+} and Fe^{3+} fixation processes in the interlayer space of the mineral than the nonclay fractions. All cation-exchanged bentonites experienced slight shifts in non-lattice bands whereas the features emerged at ~3400 and 3200 cm^{-1} are unique to the newly inserted cations. The clay dehydration up to 150 °C and then the release of the water of the cation hydration shell in the temperature range of 150–300 °C were followed by dehydroxilation between 300 and 700 °C, after which no water remains in the bentonite structure. Additional features observed at elevated temperatures were assigned to the cation migration and the collapse of the clay framework. The surface areas of the Zn- and Fe-bentonites and those of the Pb-, Cu-, Ni-, Co- and Al-bentonites were found to be much higher and lower than that of raw bentonite, respectively, which were explained by the emergence of the micropores and medium mesopores in the interlayer spacings of the samples, respectively.

1. Introduction

Clay minerals, a large family of alumino-silicate structures with a range of chemical composition, structure and surface properties, are very reactive materials due to their small grain size, large surface area, adsorption properties and chemical variability. Therefore, they are of considerable recognition in all the physical, chemical and environmental processes in soils and sediments, and frequently control them [1–5]. The industrial application of clays is enormous and grows with our ability to engineer their properties and use them in the production of composite materials [6–10]. In addition, clays are able to retain inorganic and organic pollutants, and to stop the circulation of contaminated fluids in both aquatic and soil environments [11–13].

Montmorillonite, a dioctahedral clay with the 2:1 layer linkage, has a high cation-exchange capacity (CEC) ranging from 70 to 130 meq/100 g, most of which is due to the isomorphous substitution of its main cations, Si^{4+} and Al^{3+} within the structure with cations of lower valency, but a lesser amount is due to the charges at the edge of the sheets [14,15]. The cation substitutions mainly take place in the octahedral sheets and may induce an enormous change in the physicochemical properties of clay minerals [16–20]. The use of modified clays with traditional clays as low-cost, effective catalyst materials for the removal of metal ions from industrial effluents and wastewaters through ion exchange or surface complexation has been of great relevance for both applications and our understanding of natural processes [21–27].

In present work, X-ray powder diffraction (XRPD), attenuated total reflection (ATR) spectroscopy, thermal analysis (DTA/TG) and surface area measurement (BET) techniques were employed to characterise Pb-, Cu-, Ni-, Co-, Zn-, Al- and Fe-bentonites, which were derived from Ca-exchanged bentonite samples.

2. Experimental

2.1. Materials

NaCl (Sigma, 99.5%), $CaCl_2{\cdot}6H_2O$ (Merck, 99.0%), $CoCl_2{\cdot}6H_2O$ (Merck, 98.0%), $CuCl_2{\cdot}2H_2O$ (Merck, 99.9%), $NiCl_2{\cdot}6H_2O$ (Merck, 99.9%), $FeCl_3{\cdot}6H_2O$ (Merck, 98.0%), $AlCl_3{\cdot}6H_2O$ (Merck, 99%), $PbCl_2$ (Merck, 99.9%) and $ZnCl_2$ (Merck, 99.9%) were used for preparing the cation-exchanged Unye bentonite samples.

2.2. Preparation of Na- and Ca-bentonite samples

Chemical composition of Unye bentonite (UB) which is an important mineral resource of Turkey was given in Table 1. 5 g of raw UB was washed with deionized water several times and dried at

* Corresponding author. Tel.: +90 362 3121919; fax: +90 362 4576081.
E-mail address: bafsin@omu.edu.tr (B. Afsin).

1385-8947/$ – see front matter © 2008 Elsevier B.V. All rights reserved.
doi:10.1016/j.cej.2008.10.028

Table 1
Chemical analysis results of raw Unye bentonite.

Constituent	SiO_2	Al_2O_3	Fe_2O_3	CaO	MgO	Na_2O	K_2O
Constituent (%)	62.0	20.10	2.16	2.29	3.64	0.27	2.53

105 °C and then centrifuged. The bentonite sample was homoionized by treating with 100 ml of 0.1 M NaCl and $CaCl_2$ solutions separately. The Na- and Ca-bentonite products thus obtained were dried at 105 °C and sieved to 38–108 μm and then kept for other experimental procedures. The CEC value of UB was determined as 74 meq/100 g clay by methylene blue adsorption technique [28].

2.3. Preparation of cation-exchanged bentonites

The Ca-bentonite sample prepared as described above was treated with 100 ml of 0.1 M $MCl_x{\cdot}nH_2O$ (M:Pb^{2+}, Cu^{2+}, Ni^{2+}, Co^{2+}, Zn^{2+}, Al^{3+}, Fe^{3+}) solutions at room temperature for 24 h under vigorous stirring. The products were washed with deionized water thoroughly and the supernatants were filtered off and the solid parts were washed with deionized water repeatedly until a negative chloride test was obtained. The solid precipitates were ground to the initial size and kept for spectroscopic measurements.

2.4. Characterization of the bentonite samples

ATR spectra of the raw and cation-exchanged bentonite samples were recorded on a Bruker Vertex 80 V-spectrometer equipped with a MCT/A detector in the region 4000–400 cm^{-1} at a resolution of 4 cm^{-1}. XRPD patterns were taken at ambient temperatures by the use of a Rigaku 2000 automated diffractometer using Ni filtered Cu Kα radiation (λ = 1.54050 Å; 40 kV and 40 mA). Bragg's law, defined as $n\lambda = 2d\sin\theta$, was used to compute the crystallographic spacing (d) for the examined bentonite samples. Thermal analysis runs were performed simultaneously on a PYRIS Diamond TG/DTA apparatus (range: 20–1000 °C) under dynamic nitrogen atmosphere at a heating rate of 10 °C min^{-1}. Calcinated α-alumina was taken as the reference. Surface areas were measured by adsorption of a special gas mixture (30% N_2 + 70% He) at 77 K using Quantachromosorb. All the samples were outgassed at 120 °C for 2 h prior to the surface area measurements.

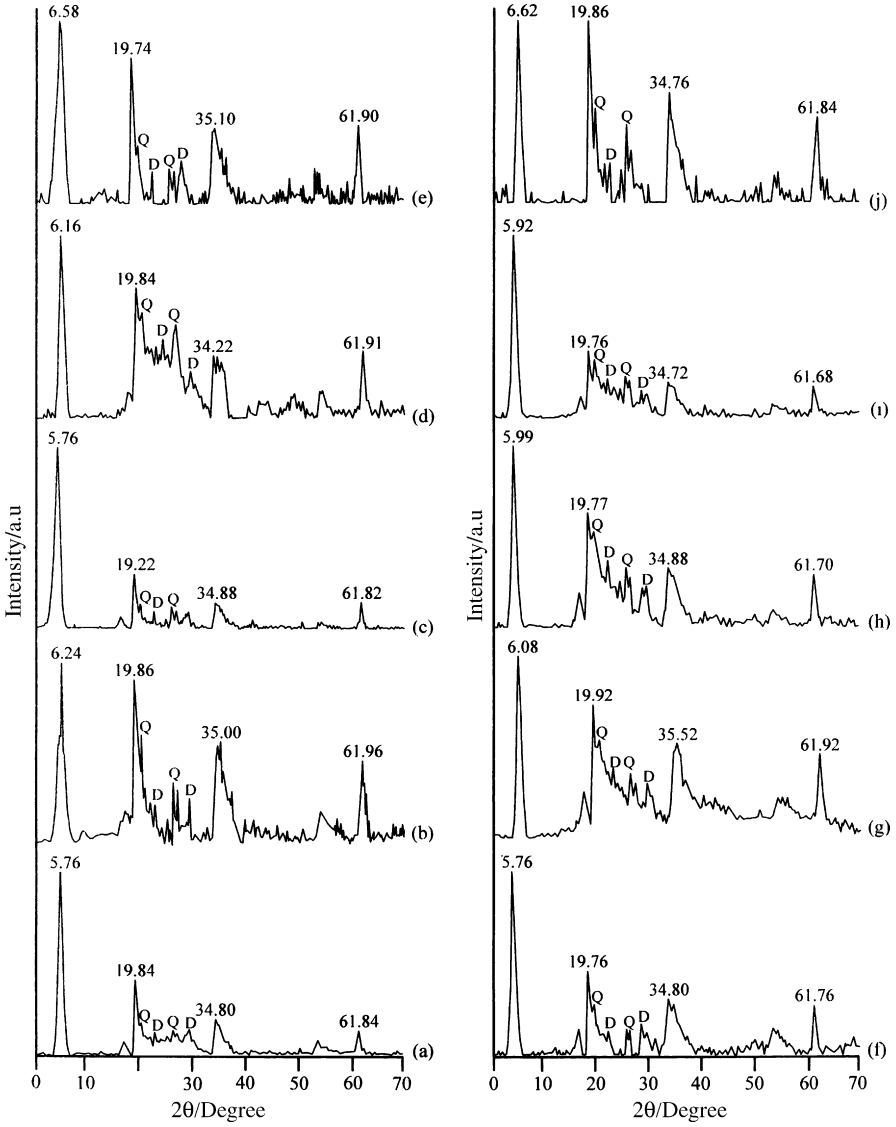

Fig. 1. XRPD patterns of (a) raw bentonite, (b) Na-bentonite, (c) Ca-bentonite, (d) Pb-bentonite, (e) Cu-bentonite, (f) Ni-bentonite, (g) Co-bentonite, (h) Zn-bentonite, (i) Al-bentonite, and (j) Fe-bentonite.

Table 2
XRPD data of raw Unye bentonite.

Diffraction plane	2θ	d (Å)	Intensity (%)	Peak area (%)
0 0 1	5.76	15.33	100	100
0 0 3	17.60	5.03	7.2	8.3
0 2 0–1 1 0	19.84	4.47	43.1	37.8
Quartz (1 0 0)	20.88	4.25	2.6	0.4
Dolomite (1 0 2)	23.43	3.79	6.1	1.8
Quartz (1 0 1)	26.81	3.32	5.2	3.8
Dolomite (1 0 4)	29.83	2.99	6.5	6.1
1 3 0–2 0 0	34.80	2.58	20.2	27.5
0 6 0–0 3 3	61.84	1.50	11.1	7.5

3. Results and discussion

3.1. XRPD data of raw and cation-exchanged bentonites

The d_{001}, d_{003}, $d_{020–110}$, $d_{130–200}$ and d_{060} diffractions of the main montmorillonite (M) component of raw UB are seen at 5.76, 17.60, 19.84, 34.80 and 61.84(2θ) with the distances of 15.33, 5.03, 4.47, 2.58 and 1.50 Å, respectively (Fig. 1a and Table 2). The peaks originating from the nonclay components (quartz (Q) and dolomite (D)) are observed at 20.88 and 26.81(2θ) with the d_{100} and d_{101} values of 4.25 and 3.32 Å and at 23.43 and 29.83(2θ) with the d_{102} and d_{104} values of 3.79 and 2.99 Å, respectively. It may be concluded from the comparison of the intensities of the d_{001} peak of raw UB and the diffractions of the nonclay components that the main component of bentonite is montmorillonite and the quartz and dolomite fractions are small. The high Mg and Ca contents of the raw bentonite (Table 1) illustrate the significant amount of Mg^{2+} and Ca^{2+} contribution from dolomite to the framework Mg and interlayer Ca cations whereas the higher d_{001} distance of raw UB (15.33 Å) than that of Na-montmorillonite (12.04 Å) and the basal spacing values varying in the range 14.45–15.40 Å may be explained by the presence of a calcium-rich bentonite sample [29]. However, the absence of the d_{001} peak at 9.98 Å in the XRPD pattern (Fig. 1a) and the lack of characteristic illite vibrations in the ATR spectrum of raw UB (Fig. 2a) rule out the presence of illite in the structure despite its low sodium content [30]. The d_{060} peak which is an important feature used for identifying the type of smectites is located at 1.50 Å in the XRPD pattern of raw UB (Fig. 1a and Table 1) revealing that the bentonite sample is an Al-rich 2:1 dioctahedral montmorillonite [31]. In addition, it may be concluded referring to the highly intensive $d_{020–110}$ features of the sample that Al is highly available in the octahedral centres of UB [32].

The d_{001} peak of 15.33 Å at 5.76(2θ) of raw bentonite shifts to 6.16(2θ) (the distance: 14.34 Å) and d_{003} peak of 5.03 Å at 17.60(2θ) appears at 18.31(2θ) with the distance of 4.84 Å in the XRPD pattern of Pb-bentonite (Fig. 1d). In addition, the d_{004} peak of 3.60 Å at 24.73(2θ) is seen and the d_{020}, $d_{130–200}$ and d_{060} peaks of montmorillonite are observed at 19.84, 34.22 and 61.91(2θ) with the distances of 4.47, 2.61 and 1.50 Å, respectively. Furthermore, the peaks from quartz are located at 20.97 and 27.20(2θ) with the distances of 4.23 and 3.28 Å and the peaks of dolomite are positioned at 23.44 and 29.85(2θ) with the distances of 3.79 and 2.99 Å, respectively. The d_{001} peak of Cu-bentonite is quite weak and a new peak of nearly the equivalent intensity with the d_{020} peak arises at 6.58(2θ) with the d value of 13.38 Å (Fig. 1e). Because of this intensity decrease, the peaks of the quartz and dolomite components become prominent in the range from 30 to 70(2θ). The insertion of nickel cations does not seem to affect the d_{001} distance of the raw bentonite and the diffraction peaks of montmorillonite emerge at 17.92, 19.76, 34.80 and 61.76(2θ) and those of quartz and dolomite are seen at 20.80 and 26.63(2θ) and 23.38 and 29.64(2θ), respectively (Fig. 1f). The d_{001} peak of Co-bentonite is located at 6.08(2θ) with a distance of 14.53 Å and the d_{003}, $d_{020–110}$, $d_{130–200}$ and d_{060} diffractions are observed at 18.16, 19.92, 35.52 and 61.92(2θ) with the distances of 4.88, 4.45, 2.53 and 1.50 Å, respectively (Fig. 1g). The peaks of the quartz and dolomite components are detected at 21.04, 23.60(2θ) and 26.96, 29.92(2θ), respectively. The d_{001} peak of Zn-bentonite is observed at 5.99(2θ) with a distance of 14.72 Å (Fig. 1h) and the other diffraction peaks of bentonite are positioned at 18.08, 19.77, 34.88 and 61.70(2θ). The diffraction peaks of quartz and dolomite are placed at 20.89, 26.88(2θ) and 23.37, 29.76(2θ), respectively. The d_{001} peak is observed as an intensified feature at 5.92(2θ) with a distance of 14.91 Å when Al^{3+} cation is introduced into the interlayer of the clay and the distances of 4.86. 4.49. 2.58 and 1.50 Å correspond to the d_{003}, $d_{020–110}$, $d_{130–200}$, and d_{060} diffractions, respectively (Fig. 1i). Furthermore, the peaks of quartz are seen at 20.96 and 26.73(2θ) and those of dolomite are located at 23.38 and 29.83(2θ). The peaks of nonclay components become prominent for Fe-bentonite due to the d_{001} peak of montmorillonite which is weaker than the (0 2 0) diffraction peak and it is observed at 6.62(2θ) with a distance of 13.10 Å (Fig. 1j). The minimum d_{001} value is unique for Fe-bentonite among all the cation-exchanged samples studied here. The variations and differ-

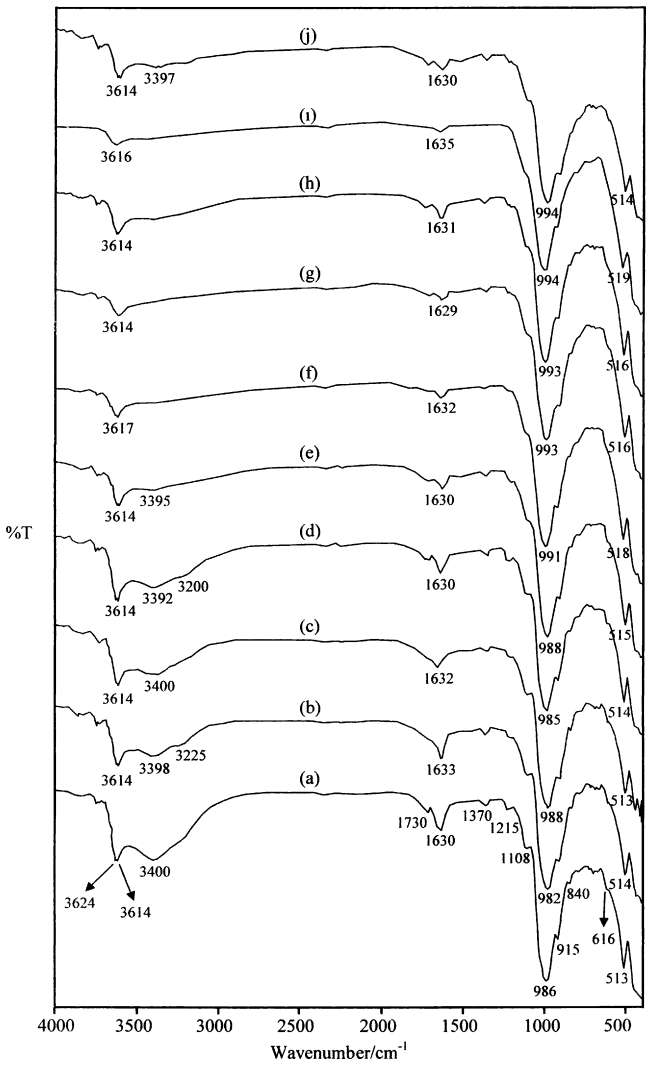

Fig. 2. ATR spectra of (a) raw bentonite, (b) Na-bentonite, (c) Ca-bentonite, (d) Pb-bentonite, (e) Cu-bentonite, (f) Ni-bentonite, (g) Co-bentonite, (h) Zn-bentonite, (i) Al-bentonite, and (j) Fe-bentonite.

Table 3
d_{001} values of raw and cation-exchanged Unye bentonite samples.

Sample	Ionic radii (Å)	d_{001} (Å)
Raw bentonite	–	15.33
Na-bentonite	0.95	14.15
Ca-bentonite	1.00	15.33
Pb-bentonite	1.20	14.34
Cu-bentonite	0.70	13.38
Ni-bentonite	0.69	15.33
Co-bentonite	0.74	14.53
Zn-bentonite	0.74	14.72
Al-bentonite	0.50	14.91
Fe-bentonite	0.56	13.10

ences in the position and the intensity of the main (0 0 1) peak drawn by the cation-exchange processes (Table 3) affected the relative intensities of the other diffraction peaks as well as nonclay peaks. This outcome which signifies that a small fraction of iron ions penetrates into the octahedral vacancies from the hexagonal cavities [13] has to be in connection with the ratio of the amount of the cation inserted inside the interlayer of bentonite and coordinated water and the electrostatic attraction between the cations and the interlayer surface planes.

3.2. ATR spectral data of raw and cation-exchanged bentonites

The structural OH vibrations and the Si—O stretches and the OH bending modes exist in the regions 3700–3200 and 1300–440 cm^{-1}, respectively, in the ATR spectrum of raw UB (Fig. 2a) [33,34]. The characteristic OH stretching vibrations observed at 3624 and 3614 cm^{-1} which originate from the AlAlOH and AlMgOH stretches, respectively, are due to the Al-rich octahedral centres of bentonite and the partial replacement of magnesium by aluminium. In addition, the envelope at 3400 cm^{-1} which belongs to the OH stretching of H-bonded water signifies the higher amount of octahedral replacement of Mg atoms than that of Fe atoms [35,36]. The features at 1730 and 1370 cm^{-1} correspond to the combinational mode and carbonate stretching peak of dolomite, respectively. The Si—O stretching peaks of quartz and silica are coincided at 789 cm^{-1} and the vibration of dolomite is overlapped by the Si—O stretching of silica at 696 cm^{-1}. Most of the changes in the cation-exchanged samples were noticed in the 3700–3000 cm^{-1} region, as the remaining part of the spectra is almost identical to the raw bentonite. All the cation-exchanged samples have a medium intensity peak around 3610 cm^{-1}, associated with the OH-group coordinated to the cations (Fig. 2b–j). The AlAlOH stretching mode and the (cation-OH) H-bonded appeared

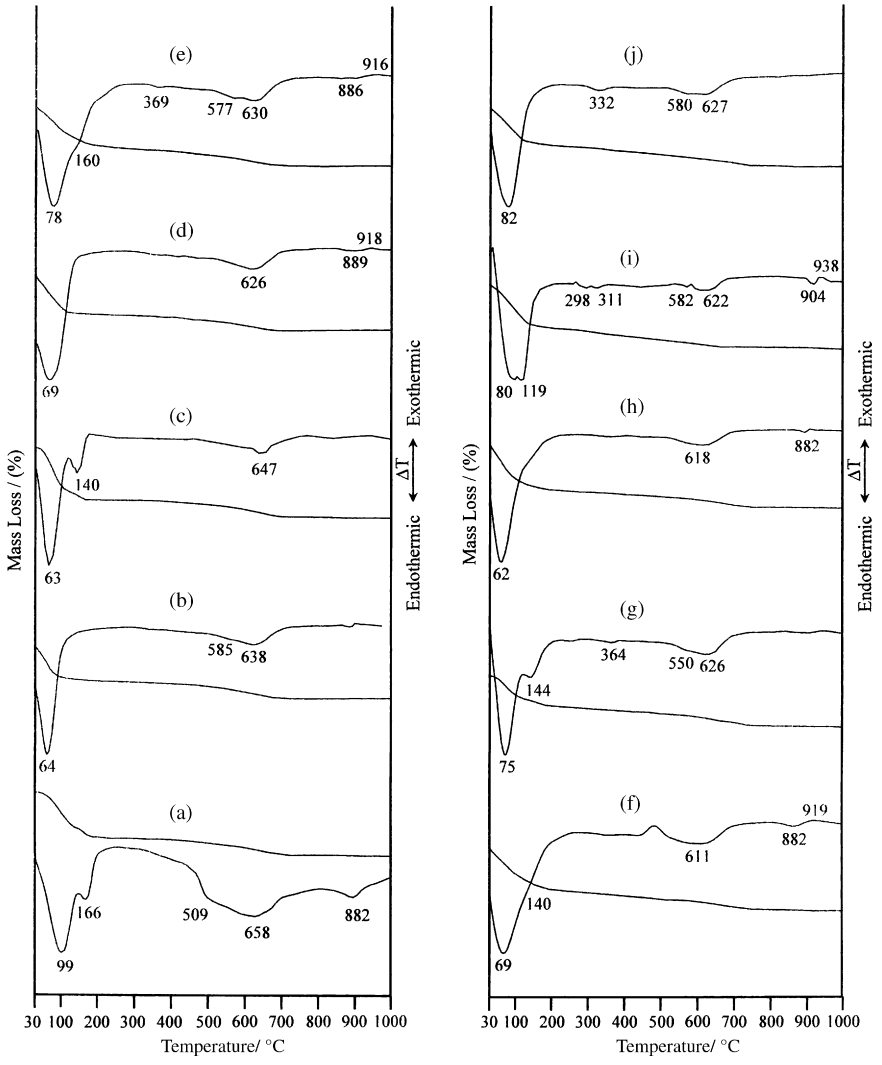

Fig. 3. DTA and TG curves of (a) raw bentonite, (b) Na-bentonite, (c) Ca-bentonite, (d) Pb-bentonite, (e) Cu-bentonite, (f) Ni-bentonite, (g) Co-bentonite, (h) Zn-bentonite, (i) Al-bentonite, and (j) Fe-bentonite.

at 3614 and 3400 cm^{-1}, respectively. The (cation-OH) H-bonded band has shifted by 5–20 cm^{-1} slightly downwards depending on the type of the exchanging cation.

A very broad envelope in the range 3500–3000 cm^{-1} consists of different features [37]. OH-groups involved in H_2O–H_2O H-bonds give rise to the vibrations around 3400 cm^{-1}, while the shoulder between 3200 and 3400 cm^{-1} is ascribed to an overtone of the H_2O bending vibration. Since H_2O molecules coordinated to the strongly polarising cations such as Al^{3+} form stronger H-bonds to water species in outer spheres of coordination, vibrations below 3200 cm^{-1} which are probably due to the M^{2+}–OH vibration are intensified (Fig. 2i) [7,34].

What appears to be important is the ratio of the peaks at 3610 and 3400–3000 cm^{-1}, as different type of cation exchange is applied. As the cations are exchanged with Ca in UB, the hydration peak intensity decreases in consistent with the fact that Ca coordinates higher amount of water than the exchanged cations (Fig. 2c–j) [38,39]. However, we refer to the new features, unique to the newly inserted cation, especially in that of Pb-bentonite, emerged at 3392 and 3200 cm^{-1} (Fig. 2d) as (cation-OH) H-stabilized species [40]. The H_2O bending mode is observed around 1630 cm^{-1}, together with the most intense peaks due to the Si—O—Si stretching modes around 990 cm^{-1} in the ATR spectra of all cation-exchanged bentonite samples (Fig. 2b–j). The (AlAlOH) and (MgAlOH) deformation peaks are found for the raw clay at 915 and 840 cm^{-1}, respectively, and at a slightly higher wavenumbers for the Na- and Ca-bentonites. It may be concluded based on the peaks above that the Al atoms are dominant in the octahedral centres of raw bentonite with a significant amount of Mg atoms. There are only minor changes in the Si—O bending vibrations at 514 cm^{-1}, due to Si—O—Al, and at 467 cm^{-1}, due to Si—O—Si, for all the samples. This is also true for the H_2O-bending mode at approximately 1630 cm^{-1}, which in all spectra consists of a shoulder which is probably due to a difference in coordination within the structure and the hydration shell [41–43]. Therefore, it is possible to provide some insight into the distinctions observed in the OH vibrational region based upon the different binding abilities of the metal cations towards the interlayer water species since the water molecule is preferably coordinated to the interlayer cations [44] and the residual water entrapped by the interlayer vacancies.

3.3. Thermal analysis data of raw and cation-exchanged bentonites

Two dehydration stages with a total mass loss of 11.2% over the temperature range of 25–220 °C are noticeable on the TG curve of raw bentonite (Fig. 3a and Table 4). The removal of adsorbed water with a mass loss of 8.1% in the first stage 25–130 °C gives rise to an endothermic DTA peak centred at 99 °C and the endothermic feature at 166 °C in the range of 130–220 °C which is accompanied by a mass loss of 3.1% corresponds to the elimination of the water species coordinated to the interlayer cations. The endothermic peak at 658 °C and the shoulder at 509 °C which are associated with the mass loss by 4.3% in the range of 300–720 °C originate from the dehydroxilation of amorphous smectites [2,33]. The endothermic maximum at 886 °C that screens the classical phase transition peak of bentonite at 910 °C represents the decomposition of dolomite impurity. The dehydration of Na-bentonite occurs with a mass loss of 8.9% in the temperature range of 30–290 °C as a single-step process which gives rise to an endothermic maximum at 64 °C (Fig. 3b) whereas this same process happens in two stages for raw bentonite. The dehydroxilation process results in two endothermic DTA peaks in the range of 290–830 °C; a strong one at 638 °C and a shoulder at 585 °C with a mass loss of 4.3%.

Table 4
Thermal analysis data of raw and cation-exchanged bentonites.

Sample	Temperature range (°C)	Mass loss (%)	DTA_{max} (endo)
Raw bentonite	25–129	8.1	99
	129–220	3.1	166
	300–720	4.3	509, 658
	720–950	0.0	910 (exo)
Na-bentonite	30–290	8.9	64
	290–830	4.3	638
Ca-bentonite	28–115	9.9	63
	115–174	2.9	140
	290–770	4.1	647
Pb-bentonite	30–290	10.0	69
	290–780	3.9	626
Cu-bentonite	30–300	10.7	78
	300–460	1.1	369
	460–600	1.6	577
	600–870	1.7	630
Ni-bentonite	30–370	12.6	69
	370–870	3.9	611
Co-bentonite	30–120	6.1	75
	120–230	2.1	144
	230–420	1.4	364
	420–880	3.7	626
Zn-bentonite	30–280	12.4	62
	280–850	4.2	618
Al-bentonite	30–105	5.8	80
	105–180	6.4	119
	200–400	1.5	298, 311
	400–750	5.2	582, 622
Fe-bentonite	30–250	10.2	82
	250–450	2.0	332
	450–600	1.8	580
	600–840	1.5	627

The endothermic maxima at 69 and 626 °C in the DTA curve of Pb-bentonite (Fig. 3d and Table 4) correspond to the removal of moisture and hydroxyl species, respectively. The amount of water removed (10.0%) is more than that of Na-bentonite and it is observed at a higher temperature whereas the hydroxyl species evolve at a lower temperature. The evolution of adsorbed and cation-coordinated water species from Cu-bentonite is represented by an endothermic peak at 78 °C and a shoulder at 160 °C, respectively, in the range of 30–300 °C with a mass loss by 10.7% (Fig. 3e and Table 4). Many researchers agree that for temperatures up to 200 °C, Cu species migrate into hexagonal cavities [13] and above 200 °C, they penetrate the octahedral sheets where they saturate the charge of the sheet [17,41,43]. Three endothermic peaks at 369, 577 and 630 °C which are accompanied by a total mass loss of 4.4% in the range of 300–870 °C signify the dehydroxilation process of Cu-bentonite [8,33]. Above 900 °C major structural changes resulting in the development of cristobalite and mullite in montmorillonite occur [15,16,42]. The removal of adsorbed and coordinated water species with a mass loss of 12.6% in the temperature interval of 30–370 °C from Ni-bentonite gives rise to a DTA peak at 69 °C and a shoulder at 140 °C (Fig. 3f and Table 4). Furthermore, the endothermic maximum at 611 °C and the shoulder at 509 °C are attributed to the dehydroxilation process.

It is clearly seen that Ni-bentonite is the sample of the minimum dehydroxilation temperature. Similar to Cu-bentonite, water and hydroxyl species desorb from Co-bentonite in two and three stages, respectively (Fig. 3g and Table 4). The adsorbed water species desorb at 75 °C; the coordinated water species are released at 144 °C, and the final dehydroxilation stage is accompanied by a peak at 364 °C, a shoulder at 550 °C and a shallow endotherm at about

Table 5
Surface areas of raw and cation-exchanged bentonites.

Sample	Surface area ($m^2\ g^{-1}$)	Ionic radius (Å)
Raw bentonite	35.0 ± 1.1	–
Na-bentonite	22.0 ± 0.7	0.95
Ca-bentonite	31.0 ± 0.9	1.00
Pb-bentonite	20.0 ± 0.6	1.20
Cu-bentonite	24.0 ± 0.7	0.70
Ni-bentonite	27.0 ± 0.8	0.69
Co-bentonite	28.0 ± 0.8	0.74
Zn-bentonite	48.0 ± 1.4	0.74
Al-bentonite	29.0 ± 0.9	0.50
Fe-bentonite	38.0 ± 1.1	0.56

626 °C. The mass losses by 12.4 and 4.2% detected in the temperature ranges of 30–290 and 290–850 °C with the endothermic maxima of 62 and 618 °C, respectively, correspond to the removal of moisture and hydroxile species, respectively, from Zn-bentonite (Fig. 3h and Table 4). The mass losses by 10.2 and 5.3% determined in the ranges of 30–250 and 250–840 °C which are accompanied by the peaks centred at 82 and 332, 580 and 627 °C, respectively (Fig. 3i and Table 4) are attributed to the elimination of the structural water and the hydration shells around iron cations as a 3-step dehydroxilation process, respectively [45,46]. It is clearly seen that the type of exchanged cation influenced significantly the thermal behavior of the bentonite samples with regard to their dehydration and dehydroxilation capacities.

3.4. Surface area measurements of raw and cation-exchanged bentonites

Higher surface area of Ca-bentonite in comparison to that of Na-bentonite (Table 5) suggests that the latter sample may have considerable amount of the trapped pores in the range of small and medium mesopores (20–400 Å) [47] and the ion valence is expected to be more important in determining the textural properties of the samples in this case. The surface areas of Pb-, Cu-, Ni-, Co- and Al-bentonite samples are interrrelated at the level of stacking of elementary layers with respect to the Fe- and Zn-samples (Table 5) in that the adsorption by reaction with the planar sites and the consequent formation of outer-sphere complexes is likely to occur [48]. The insertion of iron and zinc cations into UB reduces the number of medium and large mesopores (>100 Å) and thus, the exchange process results in significant increase in the surface areas of Fe- and Zn-bentonites with respect to the raw bentonite sample. The amount of the trapped pores in both Zn- and Fe-bentonite samples is lower than those of the Pb-, Cu-, Ni-, Co-, and Al-exchanged ones which can be explained by the emergence of micropores (<20 Å) as a result of the arrangement of zinc and iron cations in the interlayer spacing of these sample [7]. Obviously, lead, copper, nickel, cobalt and aluminium cations are subjected to compact packing in the interlamellar layer resulting in more serious pore blocking that inhibits the passage of nitrogen molecules [49]. These findings suggest that the zinc and iron ions are introduced inside the interlayer of the clay mineral not only by cation exchange at the planar sites, but also through the interaction with the aluminosilicate sheets [41]. Accordingly, the increase of the surface area induced by the incorporation of zinc and iron ions between the silicate layers is mainly caused by the presence of the micropores produced in the interlayer spaces. However, the diffuse negative charge which is less accessible in the octahedral sheets than the tetrahedral ones leads to the greater capacity to form inner-sphere complexes at the edge sites for iron species [47]. Hence, a smaller increase in the surface area of Fe-bentonite is closely related to the arrangement and amount of iron cation in the interlayer of bentonite rather than the ionic radius [25]. The above results indicate that the exchanged ions affect the surface characteristics of bentonite in some manner that appears to be related to the size and interlayer arrangement of the exchanged ion in the clay [50]. It may be concluded therefore that the order of the surface area increase of the cation-exchanged UBs is directed by the features of the clay minerals rather than the chemical properties of the metal ions [11,49].

4. Conclusions

Both the XRPD pattern and the ATR spectrum prove that the raw bentonite sample is an Al-rich dioctahedral montmorillonite. The d_{001} distances of cation-exchanged bentonites fall in the range of 13.10–15.33 Å. There appeared significant differences between the surface characteristics of the different cation-exchanged bentonites. It is generally seen from the thermal analysis (DTA/TG) data of raw and cation-exchanged UB samples that the distinct dehydration stages of low temperatures associated with adsorbed and cation-coordinated water species are followed by dehydroxylation at intermediate temperatures which ceased around 700 °C and then the phase transition occurs. Furthermore, external clay components and impurities may also be exposed to thermal decomposition at relatively high temperatures. In general, the surface areas of the cation-exchanged bentonites are found to be smaller than that of raw bentonite. However, the surface area increase of the Fe-bentonite and in particular that of Zn-bentonite comparing to that of raw bentonite is of significance and the changes in the surface characteristics of the samples are closely related to the arrangement of the cations in the interlayer. Considerable percentage of the surface area is associated with mesopores in Pb-, Cu-, Ni-, Co- and Al-bentonite samples whereas Fe^{3+} and Zn^{2+} cations generate large number of micropores and thus, induce the shrinkage of interlamellar cavities. The outcoming results of this study may be useful for predicting the potential of Unye bentonite in view of its application for the removal of metal ions from contaminated effluents. The results of such studies can also be of use in order to acquire more information on the surface properties of clay minerals and to gain insight into the behavior of cation-exchanged clay minerals in natural systems.

Acknowledgment

Research Foundation of Ondokuz Mayis University is acknowledged for the financial support to this work under the Project Number F467.

References

[1] P.L. Hall, Clays: their significance, properties, origins and uses, in: M.J. Wilson (Ed.), A Handbook of Determinative Methods in Clay Mineralogy, Blackie, Glasgow, 1987, pp. 1–25.
[2] M.S. Hassan, N.A. Abdel-Khalek, Benefication and applications of an Egyptian bentonite, Appl. Clay Sci. 13 (1998) 99–115.
[3] R.J. Morris, D.E. Williams, H.A. Luu, C.F.B. Holmes, R.J. Andersen, S.E. Calvert, The adsorption of microcystin-LR by natural clay particles, Toxicon 38 (2000) 303–308.
[4] G.J. Churchman, Formation of complexes between bentonite and different cationic polyelectrolytes and their use as sorbents for non-ionic and anionic pollutants, Appl. Clay Sci. 21 (2002) 177–189.
[5] Y. Huang, X. Ma, G. Liang, H. Yan, Adsorption of phenol with modified rectorite from aqueous solution, Chem. Eng. J. 141 (2008) 1–8.
[6] I.E. Odom, Smectite clay minerals: properties and uses, Philos. Trans. R. Soc. Lond. A 311 (1984) 391–409.
[7] C.C. Wang, L.C. Juang, C.K. Lee, T.C. Hsu, J.F. Lee, H.P. Chao, Effect of exchanged surfactant cations on the pore structure and adsorption characteristics of montmorillonite, J. Colloid Interface Sci. 280 (2004) 27–35.
[8] A. Tabak, B. Afsin, S.F. Aygun, H. Icbudak, Phenanthroline Cu(II)-bentonite composite characterization, J. Therm. Anal. Cal. 81 (2005) 311–314.
[9] B. Caglar, B. Afsin, A. Tabak, Benzamide species retained by DMSO composites at a kaolinite surface, J. Therm. Anal. Cal. 87 (2007) 429–432.

[10] J. Cuadros, Clay as sealing material in nuclear waste repositories, Geol. Today 24 (2008) 99–103.
[11] S.E. Bailey, T.J. Olin, R.M. Bricka, D.D. Adrian, A review of potentially low-cost sorbents for heavy metals, Water Res. 33 (1999) 2469–2479.
[12] S.M. Shevchenko, G.W. Bailey, L.G. Akim, The conformational dynamics of humic polyanions in model organic and organo-mineral aggregates, J. Mol. Struct.: Theochem. 460 (1999) 179–190.
[13] H.P. He, J.G. Guo, X.D. Xie, J.L. Peng, Location and migration of cations in Cu^{2+}-adsorbed montmorillonite, Environ. Int. 26 (2001) 347–352.
[14] G. Brown, Crystal structures of clay minerals and related phyllosilicates, Philos. Trans. R. Soc. Lond. A 311 (1984) 221–240.
[15] M.F. Brigatti, E. Galan, Structures and mineralogy of clay minerals, in: F. Bergaya, B.K.G. Theng, G. Lagaly (Eds.), Handbook of Clay Science, Developments in Clay Science, vol. 1, Elsevier, Amsterdam, 2006, pp. 19–86.
[16] M.L. Occelli, R.M. Tindwa, Physicochemical properties of montmorillonite interlayered with catonic oxyaluminum pillars, Clays Clay Miner. 39 (1983) 22–28.
[17] M. Stadler, P.W. Schindler, Modeling of H (super +) and Cu (super 2+) adsorption on calcium-montmorillonite, Clays Clay Miner. 41 (1993) 288–296.
[18] J. Comets, L. Kevan, Adsorption of ammonia and pyridine on copper(II)-doped magnesium-exchanged smectite clays studied by electron spin resonance, J. Phys. Chem. 97 (1993) 466–469.
[19] R. Van Bladel, H. Halen, P. Cloos, Calcium–zinc and calcium–cadmium exchange in suspensions of various types of clays, Clay Miner. 28 (1993) 33–38.
[20] T. Matsuda, K. Yogo, C. Pantawong, E. Kikuchi, Catalytic properties of copper-exchanged clays for the dehydrogenation of methanol to methyl formate, Appl. Catal. A 126 (1995) 177–186.
[21] J. Wagner, H. Chen, B.J. Brownawell, J.C. Westall, Use of cationic surfactants to modify soil surfaces to promote sorption and retard migration of hydrophobic organic compounds, Environ. Sci. Technol. 28 (1994) 231–237.
[22] M.F. Brigatti, F. Corradini, G.C. Franchini, S. Mazzoni, L. Medici, L. Poppi, Interaction between montmorillonite and pollutants from industrial waste-waters: Exchange of Zn^{2+} and Pb^{2+} from aqueous solutions, Appl. Clay Sci. 9 (1995) 383–395.
[23] M. Auboiroux, P. Bailif, J.C. Touray, F. Bergaya, Fixation of Zn^{2+} and Pb^{2+} by a Ca-montmorillonite in brines and dilute solutions: preliminary results, Appl. Clay Sci. 11 (1996) 117–126.
[24] G. Sheng, S. Xu, S.A. Boyd, Mechanism(s) controlling sorption of neutral organic contaminants by surfactant-derived and natural organic matter, Environ. Sci. Technol. 30 (1996) 1553–1557.
[25] E.Á. Ayuso, A.G. Sánchez, Removal of heavy metals from waste waters by natural and Na-exchanged bentonites, Clays Clay Miner. 51 (2003) 475–480.
[26] O. Abollino, A. Giacomino, M. Malandrino, E. Mentasti, Interaction of metal ions with montmorillonite and vermiculite, Appl. Clay Sci. 38 (2008) 227–236.
[27] K.G. Bhattacharyya, S.S. Gupta, Adsorption of a few heavy metals on natural and modified kaolinite and montmorillonite: a review, Adv. Colloid Interface Sci. 140 (2008) 114–131.
[28] G. Kahr, F.T. Madsen, Determination of the cation exchange capacity and the surface area of bentonite, illite and kaolinite by methylene blue adsorption, Appl. Clay Sci. 9 (1995) 327–336.
[29] S.J. Chipera, D.L. Bish, Baseline studies of the clay minerals society source clays: powder X-ray diffraction analyses, Clays Clay Miner. 49 (2001) 398–409.
[30] M. Jaboyedoff, F. Bussy, B. Kübler, P. Thelin, Illite "crystallinity" revisited, Clays Clay Miner. 49 (2001) 156–167.
[31] J. Srodon, V.A. Drits, D.K. McCarty, J.C.C. Hsieh, D.D. Eberl, Quantitative X-ray diffraction analysis of clay-bearing rocks from random preparations, Clays Clay Miner. 49 (2001) 514–528.
[32] A.R. Mermut, G. Lagaly, Baseline studies of the clay minerals society source clays: layer-charge determination and characteristics of those minerals containing 2:1 layers, Clays Clay Miner. 49 (2001) 393–397.
[33] C.G. Olson, M.L. Thompson, M.A. Wilson, Phyllosilicates, in: M.E. Sumner (Ed.), Handbook of Soil Science, CRC, Boca Raton, 2000, pp. F77–F168.
[34] W. Xu, C.T. Johnston, P. Parker, S.F. Agnew, Infrared study of water sorption on Na-, Li-, Ca-, and Mg-exchanged (SWy-1 and SAz-1) montmorillonite, Clays Clay Miner. 48 (2000) 120–131.
[35] J.T. Kloprogge, R. Evans, L. Hickey, R.L. Frost, Characterisation and Al-pillaring of smectites from Miles, Queensland (Australia), Appl. Clay Sci. 20 (2002) 157–163.
[36] J. Madejová, FTIR techniques in clay mineral studies, Vib. Spectros. 31 (2003) 1–10.
[37] B. Afsin, M. Gokdere, N. Tinkilic, Stability of hydroxy-formate species at a Pb(1 1 0) surface, Spectrochim. Acta, Part B 55 (2000) 985–990.
[38] L. Heller-Kallai, C. Mosser, Migration of Cu ions in Cu montmorillonite heated with and without alkali halides, Clays Clay Miner. 43 (1995) 738–743.
[39] J. Madejová, B. Arvaiová, P. Komadel, FTIR spectroscopic characterization of thermally treated Cu^{2+}, Cd^{2+}, and Li^{+} montmorillonites, Spectrochim. Acta, Part A 55 (1999) 2467–2476.
[40] B. Afsin, M.W. Roberts, Surface structure and the instability of the formate overlayer at a Pb(1 1 0) surface, Catal. Lett. 13 (1992) 277–282.
[41] C. Mosser, L.J. Michot, F. Villieras, M. Romeo, Migration of cations in copper(II); exchanged montmorillonite and laponite upon heating, Clays Clay Miner. 45 (1997) 789–802.
[42] A. Neaman, M. Pelletier, F. Villieras, The effects of exchanged cation, compression, heating and hydration on textural properties of bulk bentonite and its corresponding purified montmorillonite, Appl. Clay Sci. 22 (2003) 153–168.
[43] J.T. Kloprogge, E. Mahmutagic, R.L. Frost, Mid-infrared and infrared emission spectroscopy of Cu-exchanged montmorillonite, J. Colloid Interface Sci. 296 (2006) 640–646.
[44] A.M.L. Kraepiel, K. Keller, F.M.M. Morel, A model for metal adsorption on montmorillonite, J. Colloid Interface Sci. 210 (1999) 43–54.
[45] P.W. Schindler, P. Liechti, J.C. Westall, J. Neth, Adsorption of copper, cadmium and lead from aqueous solution to the kaolinite/water interface, Agric. Sci. 35 (1997) 219–230.
[46] T. Undabeytia, S. Nir, G. Rytwo, C. Serban, E. Morillo, C. Maqueda, Modeling adsorption-desorption processes of Cu on edge and planar sites of montmorillonite, Environ. Sci. Technol. 36 (2002) 2677–2683.
[47] J.F. Lee, C.K. Lee, L.C. Juang, Size effects of exchange cation on the pore structure and surface fractality of montmorillonite, J. Colloid Interface Sci. 217 (1999) 172–176.
[48] M. Auboiroux, F. Melou, F. Bergaya, J.C. Touray, Hard and soft acid-base model applied to bivalent cation selectivity on a 2:1 clay mineral, Clays Clay Miner. 46 (1998) 546–555.
[49] T. Vengris, R. Binkiene, A. Sveikauskaite, Nickel, copper and zinc removal from water by a modified clay sorbent, Appl. Clay Sci. 18 (2001) 183–190.
[50] P.G. Slade, P.A. Stone, E.W. Radoslovich, Interlayer structures of the two-layer hydrates of Na- and Ca-vermiculites, Clays Clay Miner. 33 (1985) 51–61.